The International Journal of Advanced Manufacturing Technology (2023) 124:2685–2700
https://doi.org/10.1007/s00170-022-10673-7

ORIGINAL ARTICLE

Enhanced abrasive-mixed-μ-EDM performance towards improved surface characteristics of biodegradable Mg AZ31B alloy

Rahul Davis[1] · Abhishek Singh[2] · Kishore Debnath[3] · Paulo Soares[4] · Stephan Hennings Och[5] · Anup Kumar Keshri[6] · Luciane Sopchenski[7] · Herman A. Terryn[7]

Received: 1 September 2022 / Accepted: 6 December 2022 / Published online: 17 December 2022

Abstract

The non-degradable metallic implants, such as bone screws, often act as the source of dysfunction and harmful corrosion products in the aqueous environment inside the human body. Many of these implants are fixed either temporarily or permanently into the human body, and therefore, both need to match tight tolerances with a remarkably finished surface to eradicate burrs or striations. In this regard, the new generation of degradable magnesium (Mg) alloy implants with excellent osseointegration and low elasticity (like that of human bone), minimizing stress shielding, have been identified as potential candidates to challenge surgical procedures reintervention. However, the biological response of an implant toward the cells in vivo can be predominantly regulated by modifying the surface chemistry, morphology, and corrosion characteristics. Powder or abrasive-mixed-micro-electric discharge machining (A-M-μ-EDM) is gaining attention for executing precision machining and achieving a simultaneous surface modification on micro-manufactured surfaces, suitable for clinical applications. Therefore, the present research aimed at improving the surface characteristics of Mg AZ31B alloy via an augmented performance of A-M-μ-EDM by adopting copper and brass-micro-electrodes (C-μ-E and B-μ-E) in association with distinct abrasive particle concentrations (APCs: 0, 1.5, 3, 4.5, and 6 g/l) of bioactive zinc abrasives. To enhance the A-M-μ-EDM capabilities, the experiments were designed with a one-variable-at-a-time (OVAT) strategy, and the trial runs were conducted using different combinations of μ-electrodes and APCs. The superior performance of A-M-μ-EDM was noticed with the fusion of C-μ-E and 3 g/l APC in terms of minimum machining time (MT) and dimensional deviation (DD). The additional outcomes of this work reported favorable improvements in surface morphology, chemistry, topography, wettability, microhardness, and corrosion resistance on the A-M-μ-EDMed sample of interest.

✉ Rahul Davis
rahul.davis@shiats.edu.in

✉ Paulo Soares
pa.soares@pucpr.br

Abhishek Singh
abhishek.singh@nitp.ac.in

Kishore Debnath
debnath.iitr@gmail.com

Stephan Hennings Och
stephan.och@ufpr.br

Anup Kumar Keshri
anup@iitp.ac.in

Luciane Sopchenski
Luciane.Sopchenski.Santos@vub.be

Herman A. Terryn
Herman.Terryn@vub.be

[1] Department of Mechanical Engineering, Vaugh Institute of Agricultural Engineering and Technology, Sam Higginbottom University of Agriculture, Technology and Sciences, Prayagraj 211007, India

[2] Department of Mechanical Engineering, National Institute of Technology Patna, Patna 800005, India

[3] Department of Mechanical Engineering, National Institute of Technology Meghalaya, Shillong 793003, India

[4] Department of Mechanical Engineering, Pontifícia Universidade Católica do Paraná, Curitiba, PR 80215-901, Brazil

[5] Department of Mechanical Engineering, Federal University of Paraná, Curitiba, PR, Brazil

[6] Department of Metallurgical and Materials Engineering, Indian Institute of Technology Patna, Patna 801106, India

[7] Department of Materials and Chemistry, Research Group Electrochemical and Surface Engineering, Vrije Universiteit Brussel, Brussels, Belgium

Keywords Abrasive-mixed-μ-EDM · Mg AZ31B alloy · Copper and brass-micro-electrodes · Zn abrasive particles · Machining-time · Dimensional-deviation

1 Introduction

The last two decades witnessed a notable rise in manufacturing engineered medical implants or devices such as heart valves, orthopedic implants, and orthodontic devices. These implants can be placed inside the human body on a temporary or permanent basis to diagnose, monitor, and therapeutically treat the diseased body organs or tissues, thus prolonging life's comfort, and safety. In this regard, metallic implants always gain preference over polymeric, ceramic, and composite biomaterials due to their superior load-bearing ability, biocompatibility, tensile strength, and fatigue limit [1]. However, degradable metallic implants are promising alternatives to the non-degradable ones used in temporary implant applications. For instance, degradable magnesium (Mg) alloy bone implant can avoid stress shielded through its density (1.74–2 g/cm^3), which falls near to that of human bone (1.81–2.0 g/cm^3), and thus, can potentially replace non-degradable titanium (Ti) alloy bone implant requiring to be eliminated via a second surgery after the healing of concerned damaged tissue. The non-toxic absorbability or degradation of a biocompatible Mg-based implant in the electrolytic physiological environment can assist in bone healing within an acceptable time frame [2]. However, often, as a result of unexpected variations in the corrosion rate, the degradation of a Mg implant can either be accelerated, leading to an early absorption even before the complete healing, or retarded, resulting in partial absorption even after the total recovery of the wounded tissue [3]. Besides, an implant's surface properties largely ascertain its biological reactivity and bulk material response to the human body fluids when the tissue and cells interact with the implant's surface. Therefore, these challenges with magnesium can be converted into opportunities primarily by alloying it with some adequate alloying elements and modifying the surface without altering the bulk features [4].

Further, the issue yet to be resolved for the effective utilization of magnesium alloys is their adequate machinability by conventional techniques since there is a high demand for dimensional accuracy of implants in medical settings. Another issue with magnesium alloys is controlling their degradation rate [5]. Mg and its alloys developed for medical use (such as WE (Mg-RE-Zr), ZK (Mg-Zn-Zr), and AZ (Mg–Al-Zn)), owing to their low melting point (around 650 ºC) and thus, poor durability with high-temperatures, are generally observed with discernible vibrations, irregular chip patterns, an emerged built-up edge, and increased oxidation rate (leading to increased corrosion rate), amid their conventional machining [6–8]. However, the non-traditional subtractive manufacturing approaches such as electric discharge machining (EDM) could allow the manufacturing of Mg alloys with improved geometrical features and surface properties, such as biocompatibility, as seen in Klocke's work on Mg alloy WE43 [5]. During an EDM process, the dielectric media is effectively used to control the rise in temperature while machining Mg alloys. However, based on the processing of EDM's input control factors, primarily, rapid temperature increments piloting speedy melting, and accelerated cooling rates steering the fast quenching, lead to the formation of a hard and brittle resolidified (recast) layer on the EDMed surface. In addition, the excess thickness and irregular shape of the recast layer might develop numerous micro-cracks on the EDMed surface and thus might cause an implant failure due to a substantial reduction in the resistance to abrasion, corrosion, and wear. In this regard, one of the recommended capable solutions to overcome this issue is to modify the surface by incorporating conductive metal powder (also termed as abrasive) in the conventional EDM process. The abrasive-mixed-electrical discharge machining (A-M-EDM) possesses the features to noticeably reduce the resolidified layer's size, microcracks, craters, and surface roughness [9, 10]. Kuriachen and Mathew [11] demonstrated that A-M-EDM improved the surface characteristics of Ti-6Al-4 V alloy for medical implant use. Amid the sparking process, the abrasives are aligned in a chain or bridge-like pattern, also known as the bridging effect, and enhance machinability [12]. This bridging effect charges and accelerates the abrasive particles to behave as a conductor, gathering them in arrays in the sparking zone, promoting timely discharges. This also assists in enhancing the occurrence of sparking by altering the ionization-deionization phenomenon in the dielectric, favoring the dielectric's breakdown strength, and broadening of spark gap, thus, expediting easy flushing of the debris leading to improved machinability [13].

Further, in the case of EDM of metallic biomaterials for medical implant applications, Strasky et al. [14] observed that a damaged tissue could more easily adhere and grow on an EDMed surface as a result of a simultaneous noticeable surface modification achieved during the EDM process. In addition, with the help of a review [8] and two research articles [15, 16], it was observed that this EDM-induced surface modification could significantly enhance osseointegration, biocompatibility, microhardness, and wear characteristics of the implant biomaterials. The basic mechanism of such type of surface modification via A-M-EDM includes the transfer, melting, and deposition of material either from EDM electrodes or added abrasive particles or both to the workpiece surface amid the machining process. Abdul-Rani et al. [17]

achieved a 44% better surface finish with zinc abrasive particles on Mg AZ31B alloy than the surface machined without using the same. The authors also reported that the process helped govern Mg alloy's corrosiveness. The addition of abrasives such as tantalum carbide and silicon carbide to the dielectric resulted in minimal micro-crack formation and enhanced micro-hardness and corrosion resistance [18, 19]. In addition, significant corrosion resistance and bioactivity are other attractive features of Zn abrasives, which contribute toward forming promising chemical compounds on the finally modified surface [10], leading to improved corrosion resistance and biocompatibility of Mg alloys [17, 20]. However, excess deposition of the migrated particles might considerably increase the recast layer thickness and cause short-circuiting [12]. Hence, one of the effective ways to control the same is by optimizing the consolidation of abrasives, which regulates the discharge rate by varying the gap generated in the middle of the tool electrode and the surface of the workpiece [21, 22].

Besides this, another advancement of macro-EDM and thus macro-A-M-EDM is their execution at the micro level, also termed as μ-EDM and A-M-μ-EDM, respectively. These μ-variants use comparatively lower levels of input control factors such as low-energy discharge, that consequently achieve thinner recast layer and smaller craters with less adverse effects on the workpiece materials existing desirable properties compared to a macro-A-M-EDM [23, 24]. Although both macro- and μ-EDM incorporate the same working principle using accurately controlled sparks, the major differences between the two are primarily noticed as a result of scaling-effect (ranging from several millimeters to a few microns or even nanometres) and energy or power densities (acting on the workpiece surface) [25]. μ-EDM uses significantly lower tool electrode diameter (< 999 µm), inter-electrode gap (< 10 µm), open circuit voltage (10–120 V), peak current (< 3A), pulse-on-time (50 ns—100 µs), and specific energy, compared to macro-EDM [26]. Further, in macro-EDM, the mechanism of material subtraction takes place principally in the form of melting and vaporization, whereas in μ-EDM, it is mainly via ablation. The possible reason behind the same is the dimensions of the plasma channel developed during the different discharges of macro- and μ-EDM. Although in comparison with μ-EDM, the longer pulse duration of macro-EDM leads to a bigger plasma channel, macro-EDM's bigger tool electrode (diameter > 999 µm) achieves lower energy density (due to higher energy loss via heat conduction) impacting the workpiece surface. Whereas μ-EDM's smaller tool electrode in association with a shorter pulse-duration-induced plasma channel can attain higher energy density (approximately 30 times) leading to higher material subtraction efficiency, compared to macro-EDM [27]. In this relation, Cyril et al. [28] attained a significant modification on biocompatible stainless steel 316L by using A-M-μ-EDM. A recent study considerably modified degradable Mg AZ91D alloy by A-M-μ-EDM and reported a noticeably reduced degradation rate during the corrosion test [10].

Further, based on the availability of only a few articles on A-M-μ-EDM of Mg alloys, there is still huge scope to achieve machining-induced surface modification on Mg alloys by improving the existing machining efficacy with some advanced strategies. Moreover, based on the above discussed facts covering the differences between macro- and μ-EDM, the optimized values of the input control factors of large-scale A-M-EDM may not necessarily be steady with A-M-μ-EDM. Therefore, such notions and key precepts, debated in the extant research, are required to be examined in the case of A-M-μ-EDM of Mg alloys. In addition, the inclusion of bioactive abrasive particles in association with distinct μ-electrode materials during A-M-μ-EDM of medical grade Mg alloys has been rarely investigated. Also, any significant improvement in the A-M-μ-EDM-induced corrosion resistance of Mg alloy, leading to a notable delay in its degradation, might be counted as a major novelty of this research for degradable implant applications. Hence, the undiscussed areas and unidentified facts on the micromachining of varieties of degradable Mg alloys for medical settings signalize the urgency for subsequent research. Therefore, to address the needs so far lacking in the scientific literature, the present work compared the performances of μ-electrodes made up of copper and brass (C-μ-E and B-μ-E) in association with distinct zinc abrasive particle concentrations (APCs) in terms of minimum machining-time (MT) and dimensional-deviation (DD) during A-M-μ-EDM of Mg AZ31B alloy. MT could be defined as the total time consumed in achieving the intended depth of cut, whereas DD is the divergence of the dimension of the finally achieved A-M-μ-EDMed hole from the diameter of μ-electrode. Further, the surfaces obtained in the least MTs and observed with the least DDs were analyzed to determine the possible surface modification.

2 Methodology

This section provides the details of the machining setup, workpiece, machining factors, experimentation plan, and performance measures with the help of the following three subsections:

2.1 Experimental setup

The Mg AZ31B alloy workpiece procured from Petromet Flange Inc., Mumbai, India, comprised Al (3.20 wt. %), Zn (1.30 wt. %), Mn (0.18 wt. %), Si (0.10 wt. %), Cu (0.04 wt. %), Ca (0.03 wt. %), and Mg (96.7 wt. %). The super-fine,

spherical-shaped, and dark grey tinted zinc abrasive (d50; 5 µm average particle size), exhibiting 114 W/mK thermal conductivity, 7.13 g/cm^3 density, 65.3 g/mole molecular weight, and adequate lubricity, was selected as a potential abrasive for this research. To ascertain the optimal levels of the A-M-μ-EDM's input control factors while processing the Mg AZ31B alloy workpiece, the present research conducted sequenced pilot A-M-μ-EDM trial runs, by incorporating OVAT (one-variable-at-a-time) approach [29], with a set of C-μ-E and B-μ-E (diameter: 580 µm) on the Hyper-15 (with RC-type Generator Circuit) A-M-μ-EDM setup (Table Top Type CNC machine tool, Sinergy Nano Systems) for 2 mm machining depth. The pilot testing included predetermined ranges of pulse-on-time (5–25 µs), pulse-interval (30–50 µs), capacitance (10 to 150 µF), voltage (120–220 V), current (40–55 mA), µ-TE rotation speed (250–350 rpm), and APCs (0–10 g/l). In this regard, the conclusive combination of the optimal levels of input control factors, obtaining the most remarkable outcomes, is presented in Table 1.

Figure 1 mainly presents the schematic diagram of the A-M-μ-EDM setup, displaying its major parts. Also, a close view of the machining head and tank is shown.

Primarily, the mixing of abrasive particles in the dielectric takes place using a mechanical stirrer (Remi, RQT-124 A/D). The pitched-fan type impeller (size 52 mm) attached to the stirring shaft (size 8 × 350 mm) of the stirrer, located 65 mm away from the μ-electrode (minimum diametrical distance between the cylindrical μ-electrode and stirring shaft), was used to maintain the uniformity of the abrasives in the dielectric at a rotation speed of 440–480 rpm. It also assisted to feed this abrasive-mixed dielectric constantly into the machining zone. Additionally, it helped to minimize the settling or accumulation of abrasives and debris in the machining zone and at the tank's bottom. However, the agglomeration of the abrasives and debris could not be completely eliminated using this approach. Also, the non-magnetic nature of Mg AZ31B alloy did not allow the use of permanent magnets to maximize the disassociation of the debris from the abrasive particles. In this regard, the same was attempted using a filter in the circulating system. However, to maintain the overall effectiveness of the A-M-μ-EDM process, the filter was used only for a set of three consecutive trial runs (used to obtain the response data for getting the average values), and after that, the filter was cleaned up and fresh dielectric was supplied for the next set of trial runs. However, during all the above challenges, it was hypothesized that the concentration of abrasives was maintained throughout each machining trial.

Table 1 Description of A-M-μ-EDM's input control factors and their optimal levels

Pulse-on-time (µs)	Pulse-interval (µs)	Capacitance (µF)	Voltage (V)	Current (mA)	µ-TE rotation speed (rpm)	Zinc abrasive particle concentrations (g/l)
10	40	100	160	42	300	0 1.5 3 4.5 6

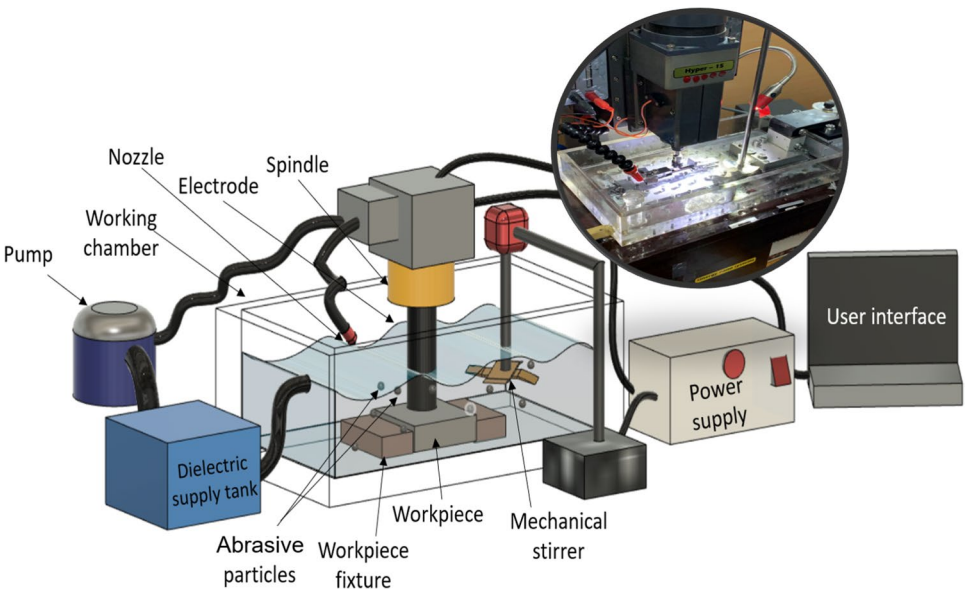

Fig. 1 Schematic diagram of A-M-μ-EDM experimental setup

2.2 Experimental plan

The OVAT method arranges the experiments under specifically restrained conditions, allowing the variation in only one (or a few) process factors at a time, and leaving others at constant values [30]. In the present work, the OVAT designed A-M-μ-EDM experimentation comprised the variation of just one input control factor at a time, with the remaining ones as constants. In this manner, the influence of each input control factor was investigated on the MT and DD three times. Later, the numeric values of these three runs were averaged and considered as the main output data. Thus, a total of 15 experimental runs (5 trials with 3 iterations) were executed with each μ-electrode.

2.3 Analyses of the outcomes

The strategic manner to investigate the A-M-μ-EDM operations and the processed samples is as follows:

2.3.1 Measurement of MTs and DDs

MTs and DDs were measured using EISCO-Digital Prostopwatch and Zeiss-Gemini 500 Field Emission-Scanning Electron Microscope (FE-SEM), respectively. Each experimental run was executed thrice, followed by averaging the measured numerical values of MTs and DDs.

2.3.2 Examination of the morphology

Further, to investigate the surface chemistry of the samples machined by C-μ-E and B-μ-E, respectively, in minimum time and displaying the least distorted shape, FE-SEM was employed to execute Energy-Dispersive X-ray Spectroscopy (EDS), followed by X-Ray Diffraction (XRD) via Shimadzu (XRD-7000) X-ray diffraction equipment with thin-film geometry. TF-XRD analysis used CuKα ($\lambda = 1.5406$ Å), 0.01° step size, 2° per minute scan speed (continuous), and 2θ range was varied between 20° to 95°, and an incident radiation angle of 5°.

2.3.3 Comprehensive investigation of the sample of interest

Based on the concluding remarks of the previous segment, the sample noticed with the best morphological characteristics was further considered for a meticulous inspection. For this reason, an attempt was made to determine the microhardness variation due to the improved morphology. The micro-indentation tests were conducted using Vickers Hardness Tester (BSHT-FHV1-50, Blue Star Ltd.) to assess the microhardness of the A-M-μ-EDMed sample of interest. Besides this, in an EDM process, the workpiece is subjected to tremendous heating during machining, followed by cooling via a dielectric. Hence, to predict the thermal behavior of the sample of interest, an attempt was made to conduct a thermal investigation in terms of temperatures and enthalpies during the phase transformations. In this relation, a DSC (Differential Scanning Calorimetry)—NETZSCH/STA 449 F3 Jupiter was employed, and the test was conducted on this sample (weighing 53.4455 mg) from 25 to 650 °C at a rate of 10 °C/min. The cooling rate controlled the solidification properties. Additionally, to develop a three-dimensional image of the sample of interest and calculate its average roughness profile (R_a), root-mean-square roughness profile (R_q), the maximum-peak-to-valley height of roughness-profile (R_t), and mean-peak-to-valley height of roughness-profile (R_z), Alicona Mex software was used with Tescan-Vega3 SEM. Further, to analyze the energy or wettability of the sample of interest, the measurement of contact angle (CA) was taken into consideration with the help of a Drop Shape Analyzer (DSA10, Krüss). The CA was achieved using a DI-water droplet of 1 μL, which was dangled from the syringe tip for a total of 60 s (with a time interval of 0.4 ms). Besides this, an electrochemical reaction induces the degradation in magnesium [4], and therefore, the corrosion resistance of the sample of interest was carried out at room temperature with the help of GAMRY Interface (1000 potentiostat/galvanostat/ZRA) — a standard cell having three electrodes. The role of counter and reference electrodes were played by graphite rod and saturated calomel electrode, respectively. Initially, the sample was polished and cleaned with acetone and ethanol, followed by proper air drying. The testing started with immersing the sample in a 3.5 wt% NaCl solution to maintain the open-circuit potential (for 60 min) of the surface of interest. Electrochemical impedance spectroscopy (EIS) measurements were executed using an amplitude of 5 mV from 100 kHz to 100 mHz at 25 °C. The equivalent electric circuit fitting was done with ZSim software ensuring a chi-squared < 0.001.

3 Results and discussion

This section presents the obtained results and their further elaboration via the following subsections:

3.1 Analysis of MTs and DDs

In the process of A-M-μ-EDM, dielectric flow is not wholly responsible for flushing the removed abrasive particles and debris because of its low pressure. The dielectric is forced to flow at small scaled machined areas by gaseous bubbles within the discharge gap for efficient flushing. However,

due to excess abrasives and debris in the discharge gap, the potent flushing is challenged by the progress in machining depth, producing a variable spark, short-circuiting, and arcing. Therefore, MT and DD often increase due to a drop in machining performance [31]. Therefore, in this regard, the observed MTs and DDs on all the A-M-μ-EDMed samples were analyzed graphically and microscopically as follows:

3.1.1 Graphical study

The OriginPro 2022 software was used to establish a graphical relationship among the various numeric values of MTs and DDs. In Fig. 2, the comparison of variations in MT and DD with changes in APCs and μ-electrodes are graphically represented and depict similar trends.

The consistent reductions were noticed in MT as well as DD with a rise in APC from 0 to 3 g/l. The rising machining temperatures facilitate a rise of conducting electrons, which could drain the dielectric's electrical resistance, weakening the breakdown strength of the dielectric in the process. The lowest values of MT and DD were obtained at 3 g/l APC mixed dielectric, displaying the most influential sparking in the machining region. The easiest machining (leading to less MT) with the least DD point towards the formation of the most effective chain-like structure or bridging among the abrasives, which, in the present work, was noticed in the case of 3 g/l APC. Therefore, 3 g/l APC possibly possessed the most influential, controlled, and frequent spark intensity, favoring the crater boundary dimensions. Also, compared to a traditional μ-EDM, an expanded discharge gap is noticed in the case of abrasive-assisted μ-EDM due to the reduced dielectric strength [10, 11]. Hence, the 3 g/l APC credibly led to the most desirable increment in the electrode gap, followed by a competent flushing of the abrasive particles

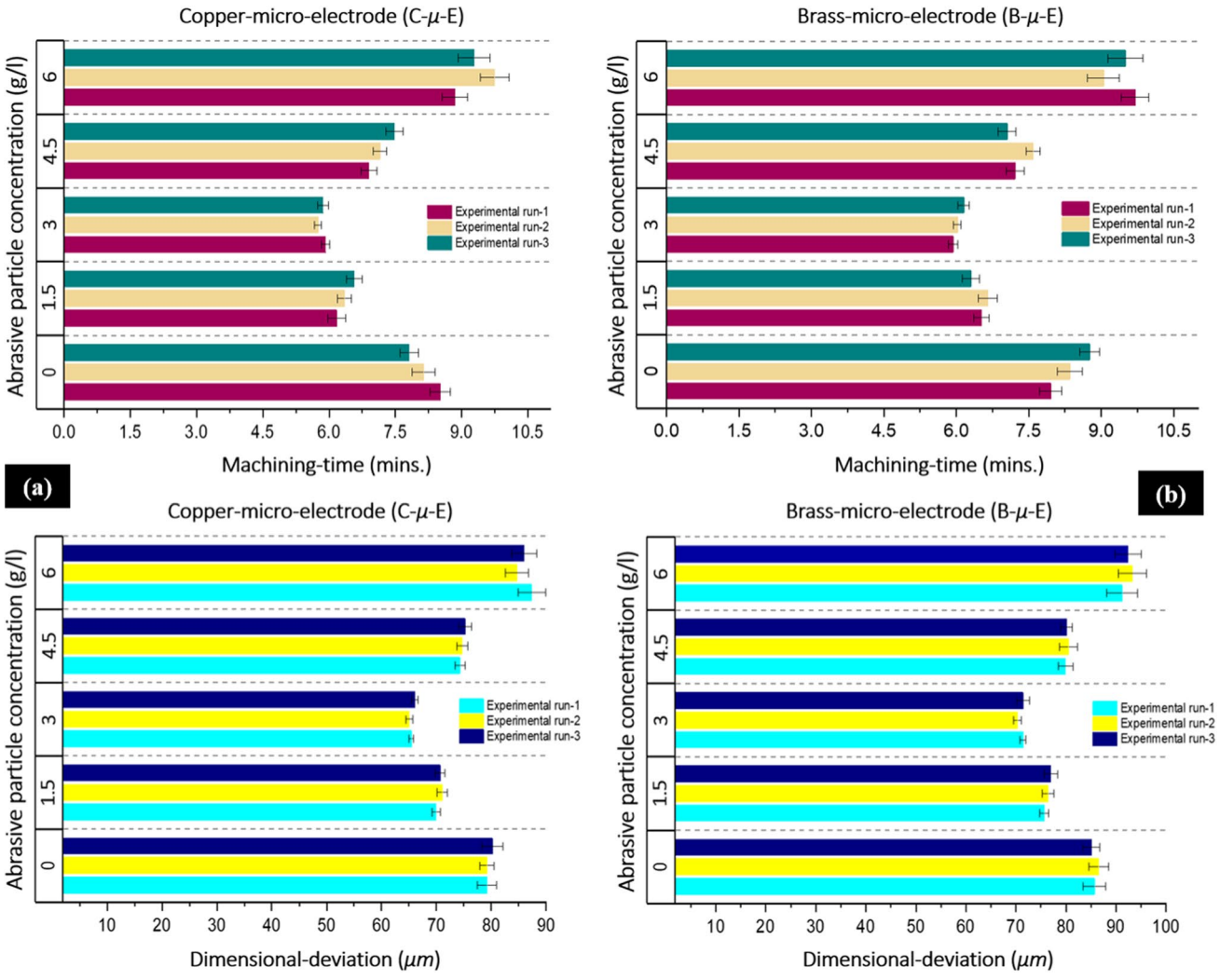

Fig. 2 Machining-time (MT) and dimensional-deviation (DD) achieved at varying APCs with (**a**) C-μ-E and (**b**) B-μ-E during A-M-μ-EDM of Mg AZ31B alloy

and melted debris. Consequently, the workpiece would be expected to experience a relatively lower discharge energy distribution because of a wide discharge gap and the presence of abrasive particles (which could absorb a notable amount of the produced heat in the discharge gap). The subsequent phenomenon would end in melting and resolidifying fewer eliminated debris, ensuring the emergence of a narrower and more uniformly dispensed solidified layer on the A-M-μ-EDMed sample's surface. Similar results were stated in some previous works [10, 21]. Additionally, the heat required for effective material subtraction was affected possibly by the interlocking among abrasive particles when the concentration went beyond 3 g/l [10, 32]. Furthermore, the probability of an unstable spark increases with the increase in machining depth, the number of debris, and APCs in the discharge gap, resulting in the reversal of μ-electrode via the feed rate control unit. Consequently, some debris and abrasive particles get settled at the deeper machining depths, which reduces the flushing effectiveness, leading to poor machining efficacy to achieve adequate MT and DD [10, 31]. Hence, these were the possible reasons why the higher APCs (4.5 and 6 g/l) achieved higher MTs and poor DDs due to the unstable performance of the μ-EDM process.

3.1.2 Microscopical measurements

Further, the various DDs (in μm) obtained on the machined workpiece by C-μ-E and B-μ-E at 0, 1.5, 3, 4.5, and 6 g/l APC were measured using the FESEM images at 200× magnification and are presented in Fig. 3a–e and f–j, respectively.

Figure 3 demonstrates those A-M-μ-EDMed samples that were noticed with the least DD after three test runs with each APC. 0 g/l APC shows machining without any addition of abrasive particles to the dielectric. The study of FESEM images revealed that the samples processed with 3 g/l APC, shown in Fig. 3c and h, respectively, were observed with the least DD in the case of C-μ-E and B-μ-E. The superior thermal conductivity (391 W/mK) and melting temperature (1087 °C) of C-μ-E over the B-μ-E (159 W/mK and 988 °C, respectively) must have induced a relatively lesser heat transfer to the machined surface, leading to lesser damage [33, 34].

3.2 Morphological examination of the A-M-µ-EDMed samples obtained at 3 g/l APC

As per the observations noticed in the previous subsection and based on the dominant performance of machining with 3 g/l APC, the present subsection focuses only on the machined samples produced with C-μ-E and B-μ-E at 3 g/l Zn APC in the least time with a minimum dimensional variation. Hence, the following segments discuss the morphological aspects of the same:

3.2.1 Microscopic assessment

FESEM was further used to assess the A-M-μ-EDMed sample surfaces of interest. In this relation, Fig. 4a presents the front and top views of the samples processed with C-μ-E, while Fig. 4b does the same for B-μ-E. It is evident that Fig. 4a and b demonstrate the developed recast layers and surface micro-cracks on the machined surfaces achieved with the two different μ-electrodes. Therefore, the performances of the C-μ-E and B-μ-E can also be distinguished in terms of the ultimately obtained solidified (recast) layer's characteristics over the A-M-μ-EDMed Mg AZ31B alloy samples. The superior thermal conductivity of C-μ-E was again credibly responsible for obtaining a thinner and more uniform recast layer with fewer thermal micro-cracks (Fig. 4a) compared to the one produced by the B-μ-E (Fig. 4b). An adequate heat transfer would eliminate a considerable volume of material from the surface being machined, causing comparatively less harm to the surface.

Hence, the material subtracted by the C-μ-E was probably more easily flushable by the dielectric, leaving a thinner recast layer behind. A substantial hike in residual thermal stress (owing to the accelerated cooling of the produced surface) and a rise in surface hardness were likely to be the reasons for surface cracking [9]. The poor thermal conductivity of the B-μ-E must have induced a relatively higher heat transfer to the machined surface, leading to greater damage of the surface (resulting in more surface micro-cracks), followed by the removal of a relatively more amount of material. Hence, upon cooling, more molten remnant material (residue) was built-up, which was difficult to be flushed, directing the development of a thicker and non-uniform recast layer. These findings are in line with previous research comprising the comparison of different EDM tool electrode materials [34].

3.2.2 EDS inspection

In addition, to characterize the elemental composition of recast layers presented in Fig. 4a and b, the EDS detected the X-rays transmitted from the A-M-μ-EDMed samples (amid the bombardment of the electron beam) and presented the spectrum of the same in Fig. 5a and b, respectively.

Both the recast layers were observed with noticeable Mg, Al, and Mn contents. In addition, the existence of Zn suggests the contribution from the workpiece itself and fused or partially melted and deposited Zn abrasive particles. Cu was possibly noticed as a result of μ-electrode wear. Additionally, both the recast layers exhibit considerable oxide contents, suggesting improved bioactivity of these two surfaces [35].

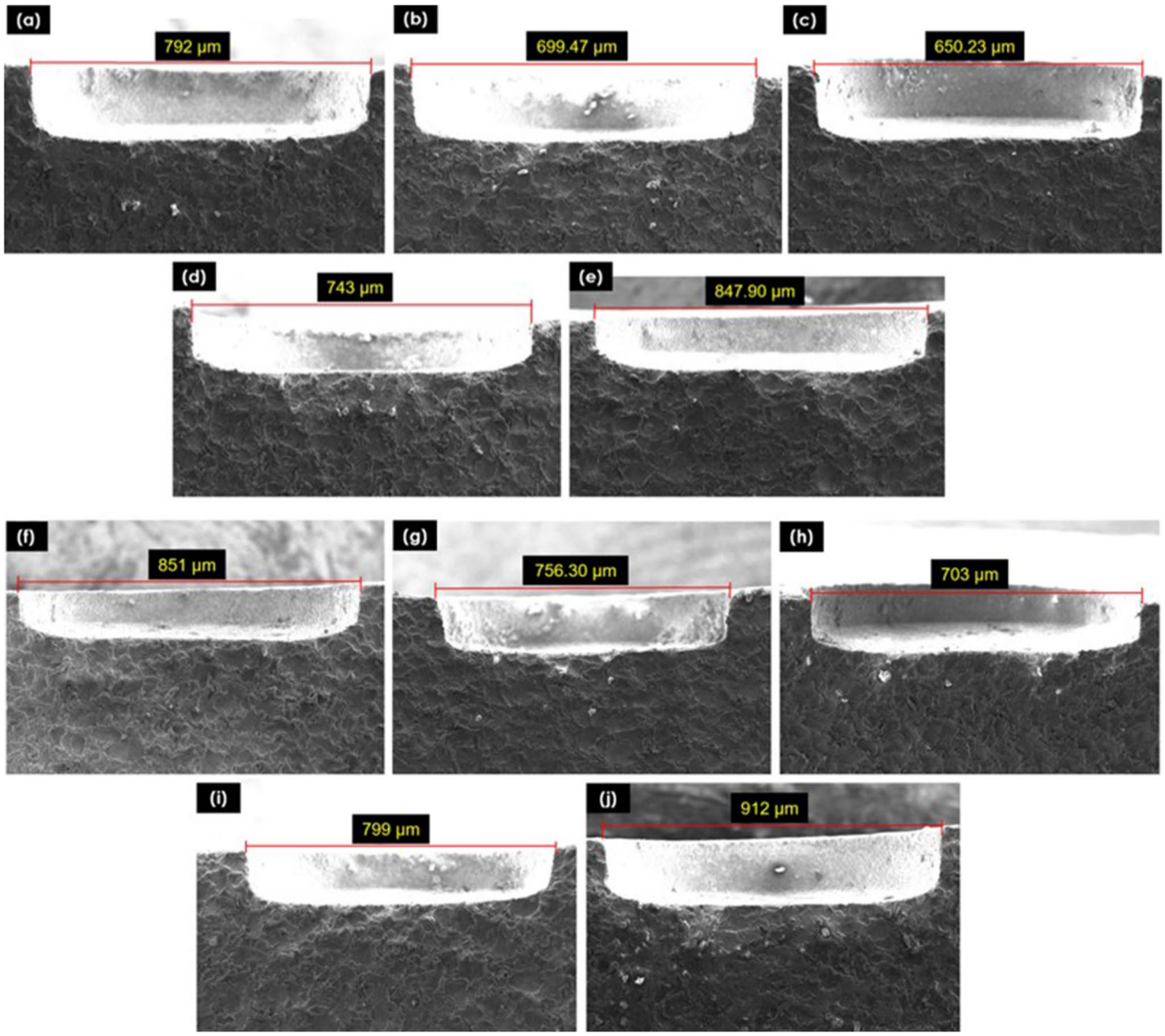

Fig. 3 Dimensional deviation observed on the A-M-μ-EDMed Mg AZ31B alloy samples with (**a**) 0, (**b**) 1.5, (**c**) 3, (**d**) 4.5, and (**e**) 6 g/l Zn APC

However, the C-μ-E achieved lesser oxide content than the B-μ-E, indicating the emergence of a recast layer with lesser thickness.

3.2.3 XRD evaluation

Further, to determine the crystalline structures developed on both the recast layers (displayed in Fig. 4a and b), their XRD studies were executed. Figure 6 shows the TF-XRD patterns of both the recast layers, where the phases α-Mg, β-$Mg_{17}Al_{12}$, ZnO, and MgO were detected. The surface machined with C-μ-E mainly exhibited α-Mg phase, with small contents of β-$Mg_{17}Al_{12}$ and ZnO.

The presence of β-$Mg_{17}Al_{12}$ suggests hindrance against corrosion due to its high passivation over many pH values [36]. MgO was probably formed due to melting near the Mg substrate. Meanwhile, the peak intensity of ZnO increased for surface machined with B-μ-E, while β-$Mg_{17}Al_{12}$ was not observed. Based on the evident oxides of zinc and magnesium, a substantial enhancement of corrosion resistance, wettability, biocompatibility, and antiviral activities on these surfaces might be expected [37,

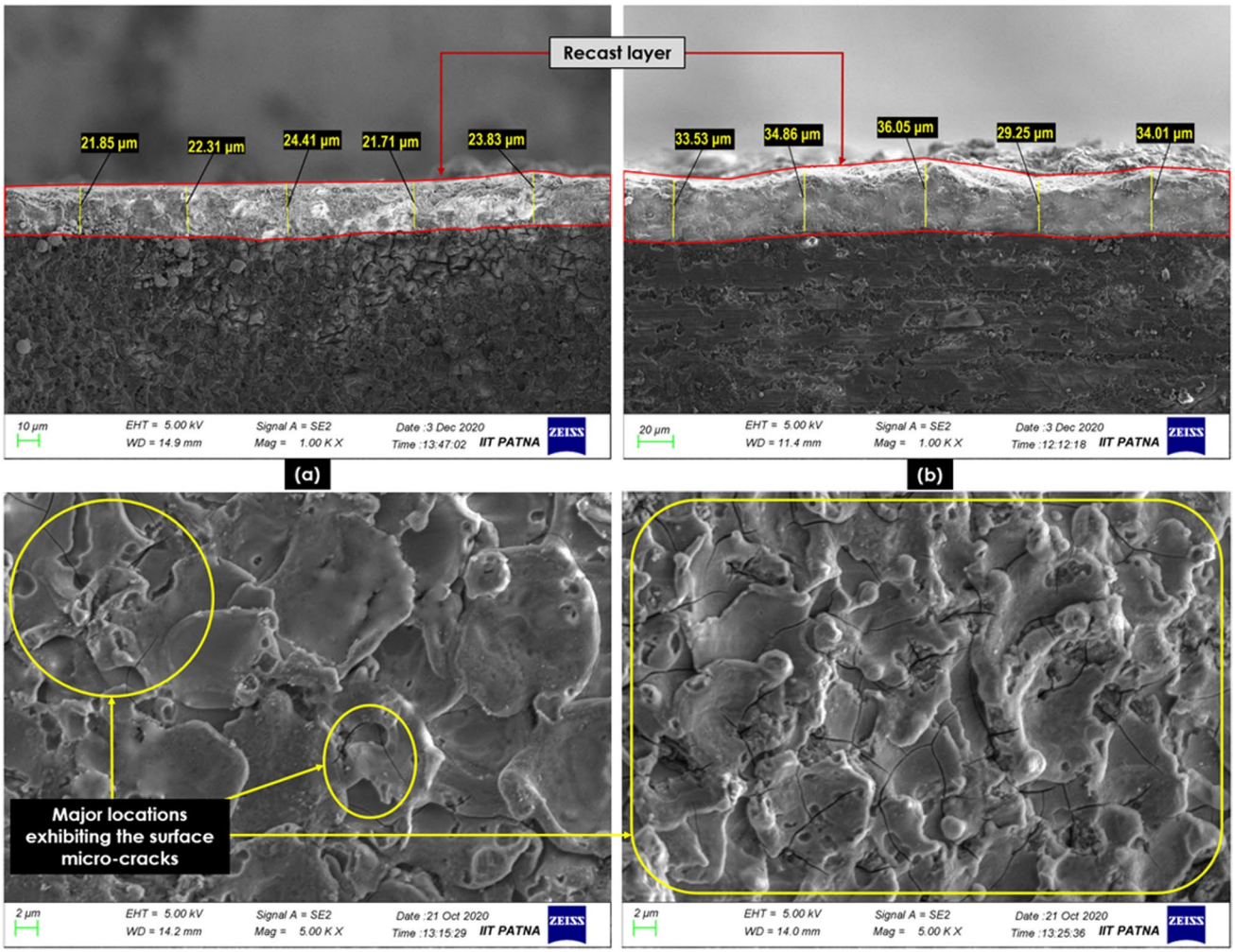

Fig. 4 Front and top views of the A-M-μ-EDMed sample surfaces of Mg AZ31B alloy obtained at 3 g/l APC with (**a**) C-μ-E and (**b**) B-μ-E

38]. The consistency in metabolic action of the host tissue might be strengthened through zinc ions against the delay in healing [39].

Besides this, in the midst of the massive destruction of lives by the severe acute respiratory syndrome coronavirus 2 (SARS-CoV-2) induced coronavirus (COVID-19), the ZnO content might act as an additional antiviral agent against coronavirus inside the body of the patient using the implant of the produced surface [40]. The various oxygen groups of Zn can potentially act as antiviral agents and cease the entry, mutation, and spread of coronavirus inside the human body [41]. However, the validation of the same was not aimed to fit in the scope of the present research. Therefore, a detailed investigation must be carried out in the subsequent research.

3.3 Detailed study of the A-M-µ-EDMed sample produced with C-µ-E at 3 g/l APC

Based on the comparative analyses presented in subsection 3.2, the sample machined with C-μ-E at 3 g/l APC was considered as the sample of relevance and interest for further investigation in the later segments of this study. Hence, the discussion on the same is as follows:

3.3.1 Microhardness and EDS elemental mapping

In this regard, the microhardness test reported that the surface of interest was detected with 49.43% higher microhardness than the as-received Mg AZ31B alloy specimen. The average value of improved microhardness was 108 HV, calculated by measuring the same at three different sites on the modified surface. The improved surface microhardness is

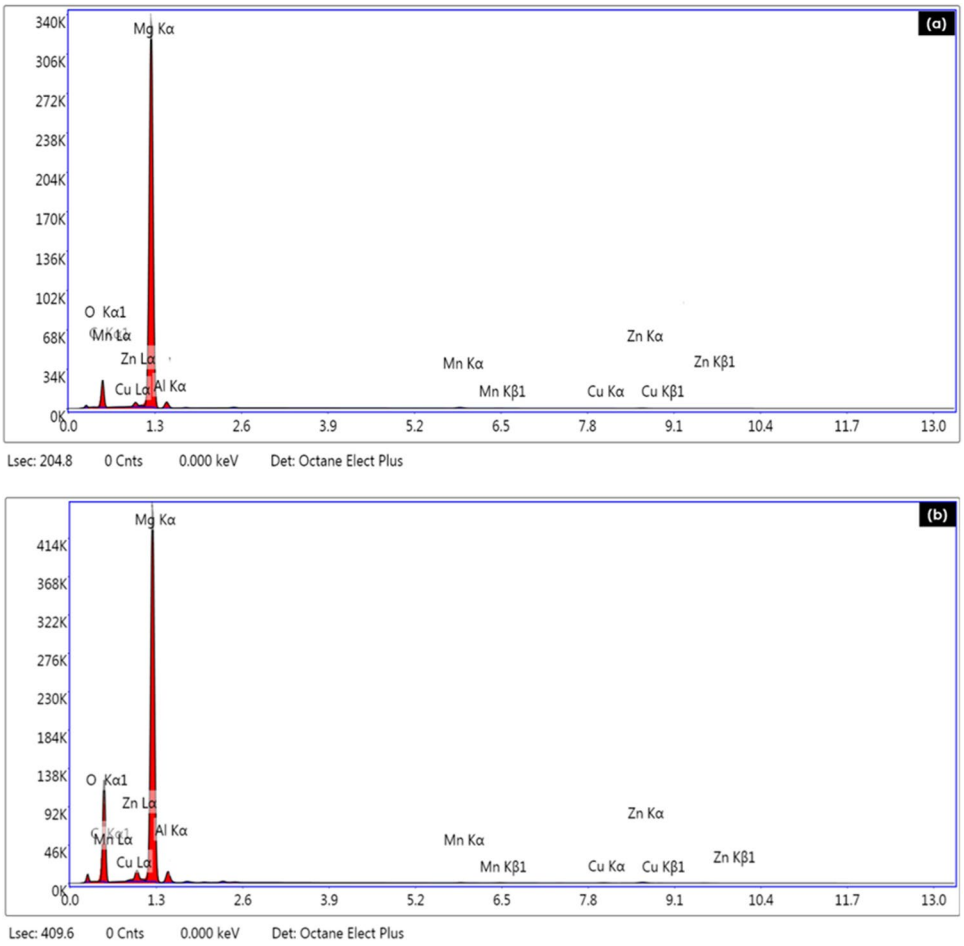

Fig. 5 EDS spectra of the recast layer detected on Mg AZ31B alloy surface after machining with (**a**) C-μ-E and (**b**) B-μ-E at 3 g/l APC

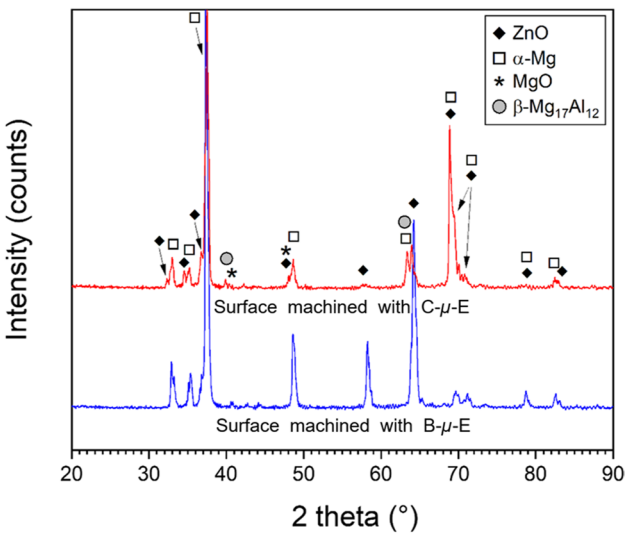

Fig. 6 TF-XRD diffractogram of the modified surfaces of Mg AZ31B alloy after A-M-μ-EDM with C-μ-E and B-μ-E at 3 g/l APC

considered an essential property of Mg alloys for medical applications [4]. As shown in Fig. 6, the possible reason for this improved microhardness might be the ample amount of oxide content. Also, the α-Mg matrix might have contributed to the formation of a part of $Mg_{17}Al_{12}$ precipitate, indicating improvement in surface microhardness [42]. Further, Fig. 7 presents the EDS elemental mapping of the modified Mg AZ31B alloy surface of interest to ascertain the percentage of elements present on this surface. The mapping revealed that this surface contained 19.24% oxide, 2.98% aluminum, 0.58% copper, and 1.08% zinc.

3.3.2 DSC response

Besides this, Fig. 8 shows the DSC response of the modified Mg AZ31B alloy surface of interest. Since the larger peak was found incomplete, the entire peak area could not be analyzed (after subtracting the baseline), and therefore, the latent heat of solidification could not be measured. Hence, the DSC spectra could predict only a qualitative behavior. Amid consistent heating, two peaks could be observed at 584 °C and 627 °C. The first peak (584 °C) could relate to

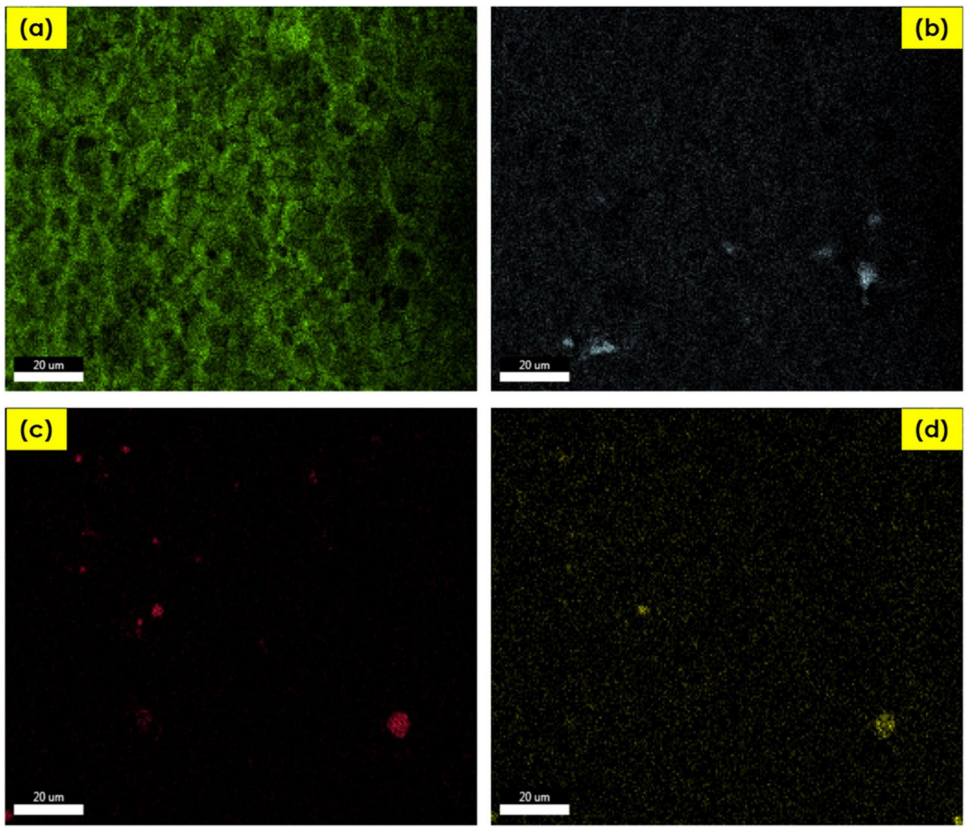

Fig. 7 EDS elemental mapping depicting (**a**) oxide, (**b**) aluminum, (**c**) copper, and (**d**) zinc

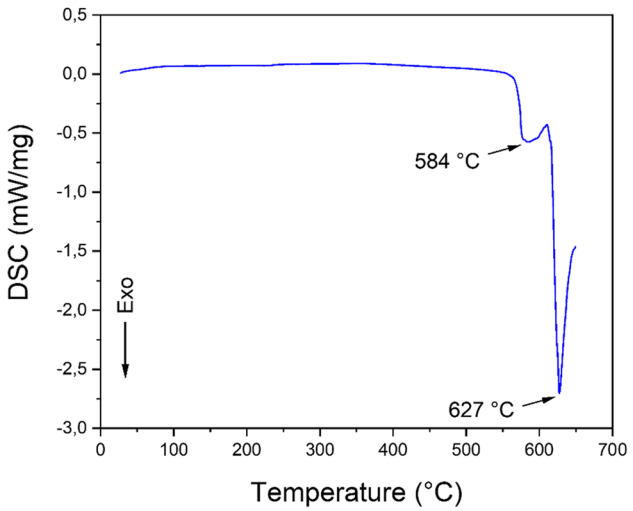

Fig. 8 DSC response of the modified Mg AZ31B alloy surface

the dissolution of the eutectic phase (Al-Mn), and the second one (627 °C) could relate to the melting of the matrix.

3.3.3 Topographic features

According to a comprehensive review, surface topographic features such as surface roughness can predict the corrosiveness and in vitro characteristics of magnesium alloys. Lower is the surface roughness, and stronger is the passivation, indicating improved corrosion resistance [43]. Hence, the corrosive characteristics of implantable Mg alloys could be ascertained to a great extent based on their topographic aspects. In this relation, this segment tested and presented the topography of the sample's surface of interest in Fig. 9. The two-dimensional (2-D) and three-dimensional (3-D) plots of the are shown in Fig. 9, where $R_a = 1.16$ µm, $R_q = 1.47$ µm, $R_t = 12.26$ µm, and $R_z = 8.29$ µm. According to a previous study, the surface topography of the order of 1 µm notably favors the in vitro cell proliferation along the groove's direction and depth of Mg alloys' implant surface [2]. Hence, the surface roughness (R_a) = 1.16 µm might be proposed as a satisfactory topographic feature for improved cell migration.

3.3.4 Wetting characteristics

Additionally, based on the wetting attributes of a surface, the adhesion, water repellency/absorption, and biocompatibility of the same can be ascertained. For this reason, the contact angle (CA) of the surface of interest is calculated as a function of the surface roughness to evaluate the wettability [44]. In this regard, the wetting characteristic of the surface of interest was achieved at

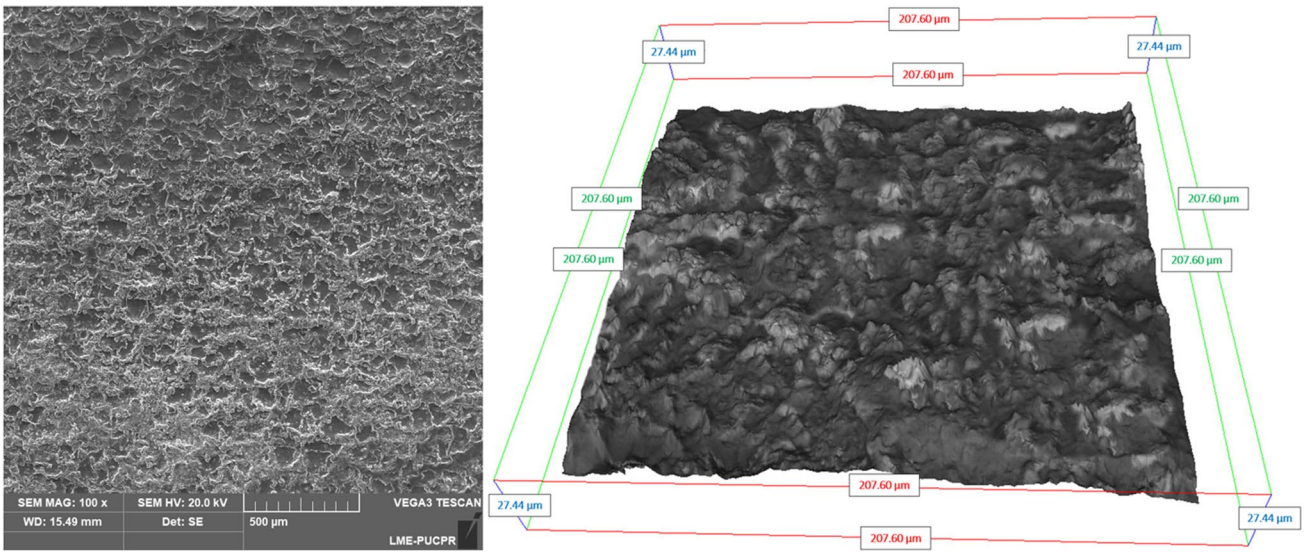

Fig. 9 2-D and 3-D view of the modified Mg AZ31B alloy surface

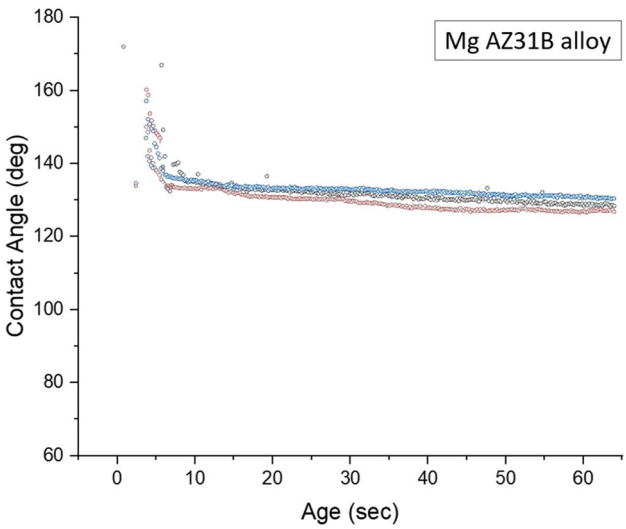

Fig. 10 Static water contact angles (CAs) as a function of time for the modified Mg AZ31B alloy

three different locations on the sample's surface and is presented in Fig. 10. These images were captured as soon as a contact between the droplet (from the syringe tip), and the machined surface gets developed. The contact angle (CA) calibrations were fit with the circle-fitting profile. From Fig. 10, the calculated value of CA was 137° (> 90°), indicating the hydrophobic behavior of the surface. The surface area/topography (with $R_a = 1.16$ µm) and surface chemistry (with considerable oxide content) were possibly responsible for the same [45]. The future scope of the present study needs to incorporate a detailed investigation of both possible reasons. Based on the R_a value of this surface (1.16 µm), the wetting is expected to be non-homogeneous since $R_a > 1$ µm [44].

According to previous research, the presence of ZnO particles might favorably affect the surface texture and increase CA, leading to improved antibacterial properties of the surface [38]. Moreover, CA > 90° suggests a comparatively inferior bio-wettability and improved degradability. Thus, the surface of interest might display favorable properties fitting for medical applications.

3.3.5 Corrosion behavior

In continuation, a subsequent corrosion test was conducted to validate the actual water repellency of this surface. Besides highlighting in vivo biocompatibility, a recent review also presented a noticeable enhancement in the corrosion behavior of Mg AZ31B alloy for bone implantation in a rabbit model [4]. In this relation, the electrochemical impedance spectroscopy (EIS) Bode and Nyquist plots of the unmachined and A-M-μ-EDMed Mg alloy samples (with and without APC) were plotted and are presented along with their fitting lines in Figs. 11 and 12. Also, in accordance with some previous studies [46–48], the experimental EIS data were fitted to an equivalent electric circuit (EEC) composed of two capacitive and one inductive loop at low frequency (as shown in Fig. 13) to display the Mg behavior in aggressive media.

The first capacitive loop (R2 and CPE) represents the charge transfer and the interfacial capacitance, whereas the second one (R3 and C) corresponds to the diffusion resistance and capacitance of the newly formed $Mg(OH)_2$, while the inductive loop (L and R4) are ascribed to the adsorption/

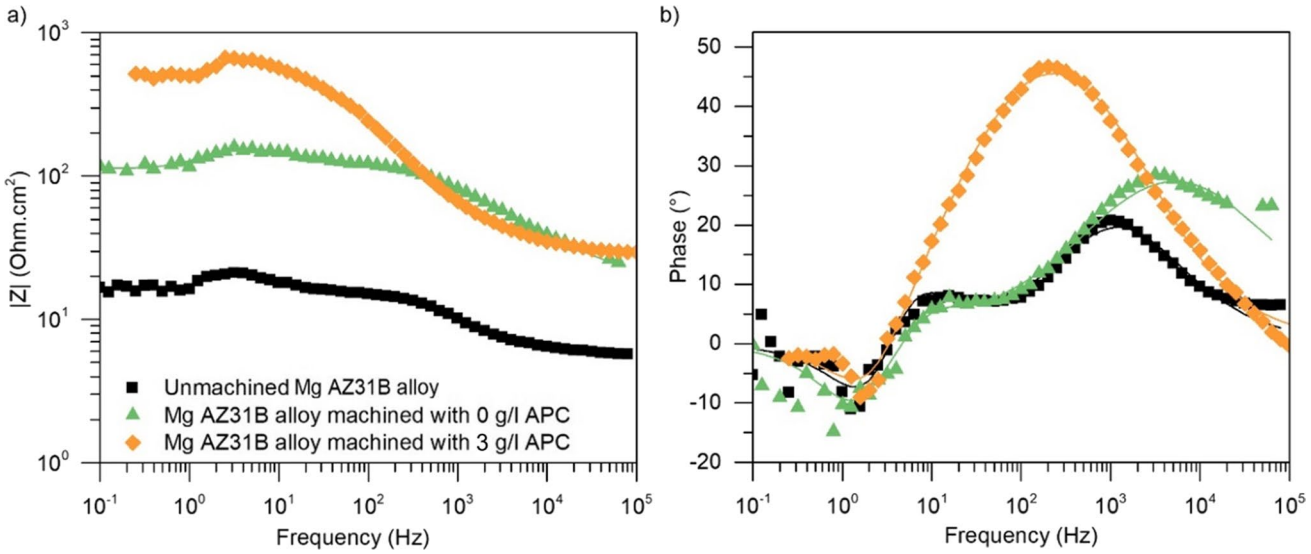

Fig. 11 Bode plot of the impedance modulus and phase of the Mg AZ31B alloy samples in 3.5% NaCl

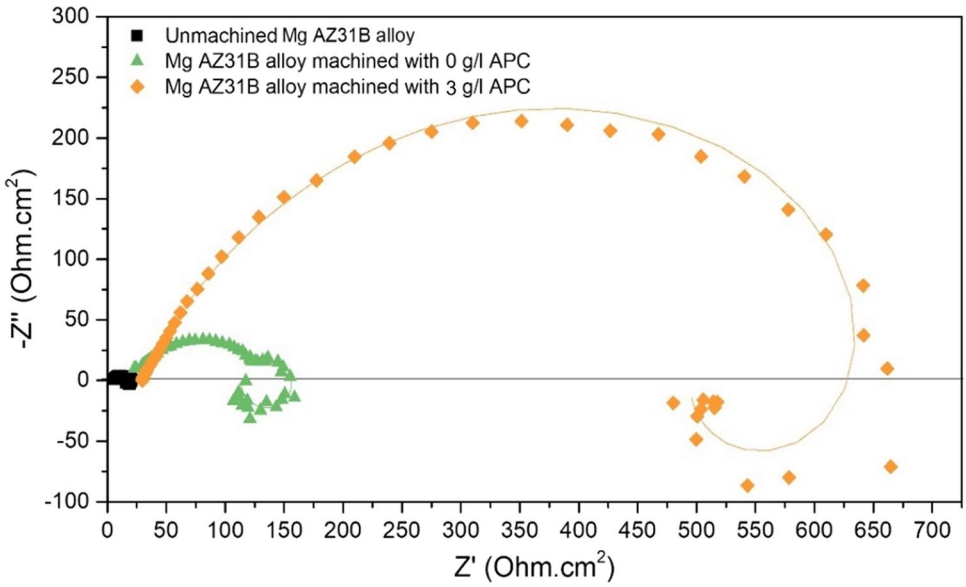

Fig. 12 Nyquist plot of the Mg AZ31B alloy samples in 3.5% NaCl

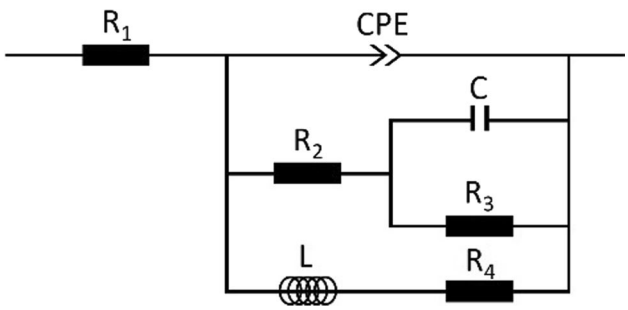

Fig. 13 Equivalent electric circuit was used to fit the EIS experimental data acquired with 3.5% NaCl

desorption of species on the sample surface. [49]. Further, in compliance with the outcomes of a previous study comprising the corrosion analysis of Mg AZ31B alloy, the values of the fitted EEC elements are shown in Table 2. In Table 2, R1 corresponds to the electrolyte resistance and Rp is the calculated resistance to polarization.

The high impedance modulus at low frequency and larger Nyquist semi-circle show that the surface modification produced by A-M-μ-EDM could substantially improve the corrosion resistance. The resistances at high and low frequencies increased considerably in comparison to the unmachined Mg alloy (R2 and R4 in Table 2). The use of

Table 2 Fitting result of the electrochemical impedance spectra of unmachined and A-M-μ-EDM machined Mg AZ31B alloy samples (with 0 and 3 g/l APC) in 3.5% NaCl

	R_1 Ohm.cm^2	CPE F.cm^{-2}.s$^{(n-1)}$	n	R_2 Ohm.cm^2	C F.cm^{-2}	R_3 Ohm.cm^2	L H.cm^{-2}	R_4 Ohm.cm^2	R_p Ohm.cm^2
Unmachined Mg alloy	5.60	2.32E-4	0.73	11.2	4.15E-3	9.13	2.27	22.39	10.65
Mg AZ31B alloy machined with 0 g/l APC	12.74	1.11E-4	0.50	147.3	–	–	52.62	308 10	99.65
Mg AZ31B alloy machined with 3 g/l APC	29.28	3.97E-5	0.71	733.7	–	–	123.80	1299.00	468.87

3 g/l APC in the machining process enhanced the overall resistance of the surface.

4 Conclusions and scope

Precision macro and micro-manufacturing have already contributed so much to advances in the medical sector and will constantly progress as an integral part of the future. Based on the interesting outcomes of this research, the following can be concluded:

- In association with 3 g/l Zn APC, C-μ-E obtained 12.51%, 14.42%, and 31.96% better MT, DD, and recast layer thickness, respectively, compared to the B-μ-E.
- When used with the C-μ-E, 3 g/l APC attained 11.48%, 14.69%, 18.55%, 16.36%, and 13.53% better MT and 11.36%, 12.98%, 16.76%, 13.43%, and 14.85% better DD at 0, 1.5, 3, 4.5, and 6 g/l APC, respectively, compared to the B-μ-E.
- XRD explains the benefits of the formed phases on the recast layer, which contributed to enhancing the overall corrosion resistance of the degradable Mg alloy.
- A-M-μ-EDM at 3 g/l APC induced resistance to polarization 4 times higher than the samples machined without the addition of abrasive particles to the A-M-μ-EDM dielectric.
- The adequate CA and corrosion resistance findings might suggest the modified surface to be used in degradable orthopedic implant applications. However, a biocompatibility test will be needed to endorse the same in successive research.
- Based on the observed Zn content on the A-M-μ-EDMed samples' surfaces (amid the morphological study), it was hypothesized that the mechanical stirrer could noticeably regulate and feed a considerable amount of Zn abrasives into the machining zone. However, the tools to monitor and facts confirming the actual amount of Zn abrasives fed into the same are yet to be investigated in future studies.
- Also, since it was hypothesized that the concentration of abrasives was maintained throughout each machining trial, an improved stirring/circulation system with a more efficient filtering arrangement is required to be developed for A-M-μ-EDM in the future research to maintain the abrasive particles' concentration in the dielectric and minimize the accumulation of debris and abrasive particles in a more effective manner.
- The subsequent research will also need to incorporate the measurement of the discharges using some device such as an oscilloscope, to confirm the intensity of the discharge energy distribution because of a wide discharge gap and the presence of abrasive particles.

Acknowledgements The authors are grateful to Mr. Hrishikesh Dutta, Mr. Ved Prakash, and Mr. Alok Kumar Mishra from the Department of Mechanical Engineering, National Institute of Technology Meghalaya, Shillong, India, Department of Materials Science and Engineering, Indian Institute of Technology Patna, Patna, India, and Department of Mechanical Engineering, National Institute of Technology Patna, Patna, India, respectively, for their technical support in this work.

Author contribution Rahul Davis: Experimental investigation, methodology, visualization, roles/writing - original draft, and writing - review and editing

Abhishek Singh: Conceptualization, formal analysis, investigation, methodology

Kishore Debnath: Execution of experimental runs and writing - review and editing

Paulo Soares: Resources, supervision, validation, roles/writing - original draft, review

Stephan Hennings Och: Metallurgical characterization of the machined surfaces

Anup Kumar Keshri: Supervision, review, and validation

Luciane Sopchenski: Execution of corrosion tests and editing

Herman A. Terryn: Analysis of corrosion tests and visualization

Data availability All the authors declare that this paper has no available data or material.

Code availability All the authors declare that this paper has no available code.

Declarations

Ethics approval Not applicable to this paper.

Consent to participate Not applicable to this paper.

Consent for publication Not applicable to this paper.

Conflict of interest The authors declare no competing interests.

References

1. Festas AJ, Ramos A, Davim JP (2020) Medical devices biomaterials – a review. Proc Inst Mech Eng Part L J Mater Des Appl 234:218–228. https://doi.org/10.1177/1464420719882458
2. Rahman M, Dutta NK, Roy Choudhury N (2020) Magnesium alloys with tunable interfaces as bone implant materials. Front Bioeng Biotechnol 8:. https://doi.org/10.3389/fbioe.2020.00564
3. Amukarimi S, Mozafari M (2021) Biodegradable magnesium-based biomaterials: An overview of challenges and opportunities. MedComm 2:123–144. https://doi.org/10.1002/mco2.59
4. Yang J, Cui F, Lee IS (2011) Surface modifications of magnesium alloys for biomedical applications. Ann Biomed Eng 39:1857–1871. https://doi.org/10.1007/s10439-011-0300-y
5. Klocke F, Schwade M, Klink A, Kopp A (2011) EDM machining capabilities of magnesium (Mg) alloy WE43 for medical applications. Procedia Eng 19:190–195. https://doi.org/10.1016/j.proeng.2011.11.100
6. Davis R, Singh A (2021) Performance study of cryo-treated end mill via wet, cryogenic, and hybrid lubri-coolant-milling induced surface integrity of biocompatible Mg alloy AZ91D. Proc Inst Mech Eng Part C J Mech Eng Sci 095440622110171. https://doi.org/10.1177/09544062211017160
7. Davis R, Singh A (2020) Tailoring surface integrity of biomedical Mg Alloy AZ31B using distinct end mill treatment conditions and machining environments. J Mater Eng Perform. https://doi.org/10.1007/s11665-020-05203-z
8. Davis R, Singh A, Jackson MJ et al (2022) A comprehensive review on metallic implant biomaterials and their subtractive manufacturing. Int J Adv Manuf Technol 120:1473–1530. https://doi.org/10.1007/s00170-022-08770-8
9. Tan PC, Yeo SH (2011) Investigation of recast layers generated by a powder-mixed dielectric micro electrical discharge machining process. Proc Inst Mech Eng Part B J Eng Manuf 225:1051–1062. https://doi.org/10.1177/2041297510393645
10. Davis R, Singh A, Debnath K et al (2021) Effect of powder particle concentration and tool electrode material amid zinc powder-mixed μEDM of biocompatible Mg alloy AZ91D. J Mater Eng Perform. https://doi.org/10.1007/s11665-021-05788-z
11. Kuriachen B, Mathew J (2016) Effect of powder mixed dielectric on material removal and surface modification in microelectric discharge machining of Ti-6Al-4V. Mater Manuf Process 31:439–446. https://doi.org/10.1080/10426914.2015.1004705
12. Patel S, Thesiya D, Rajurkar A (2016) Effect of aluminium powder concentration on powder mixed electric discharge machining (PMEDM) of inconel-718. J Mach Form Technol 8:29–40
13. Jeavudeen S, Jailani HS, Murugan M (2021) Enhancement of machinability of titanium alloy in the Eductor based PMEDM process. SN Appl Sci 3:. https://doi.org/10.1007/s42452-021-04472-0
14. Strasky J, Janecek M, Harcuba P (2011) Electric discharge machining of Ti-6Al-4V alloy for biomedical use. WDS'11 Proc Contrib Pap Part III, pp 127–131
15. Li L, Zhao L, Li ZY et al (2017) Surface characteristics of Ti-6Al-4V by SiC abrasive-mixed EDM with magnetic stirring. Mater Manuf Process 32:83–86. https://doi.org/10.1080/10426914.2016.1151043
16. Talla G, Gangopadhayay S, Biswas CK (2017) State of the art in powder-mixed electric discharge machining: a review. Proc Inst Mech Eng Part B J Eng Manuf 231:2511–2526. https://doi.org/10.1177/0954405416634265
17. Abdul-Rani AM, Razak MA, Littlefair G et al (2017) Improving EDM process on AZ31 magnesium alloy towards sustainable biodegradable implant manufacturing. Procedia Manuf 7:504–509. https://doi.org/10.1016/j.promfg.2016.12.057
18. Zain ZM, Ndaliman MB, Khan AA, Ali MY (2014) Improving micro-hardness of stainless steel through powder-mixed electrical discharge machining. Proc Inst Mech Eng Part C J Mech Eng Sci 228:3374–3380. https://doi.org/10.1177/0954406214530872
19. Ali MY, Atiqah N, Erniyati (2011) Silicon carbide powder mixed micro electro discharge milling of titanium alloy. Int J Mech Mater Eng 6:338–342
20. Hosking NC, Ström MA, Shipway PH, Rudd CD (2007) Corrosion resistance of zinc-magnesium coated steel. Corros Sci 49:3669–3695. https://doi.org/10.1016/j.corsci.2007.03.032
21. Razak MA, Abdul-Rani AM, Aliyu AA et al (2019) The potential of improving the Mg-Alloy surface quality using powder mixed EDM. Adv Struct Mater 119:43–53. https://doi.org/10.1007/978-3-030-28505-0_4
22. Peças P, Henriques E (2008) Effect of the powder concentration and dielectric flow in the surface morphology in electrical discharge machining with powder-mixed dielectric (PMD-EDM). Int J Adv Manuf Technol 37:1120–1132. https://doi.org/10.1007/s00170-007-1061-5
23. Jahan MP, Rahman M, Wong YS (2012) Study of the diffusion of carbon, its sources, and effect on finishing micro-EDM performance of cemented carbide. J Mater Eng Perform 21:1655–1668. https://doi.org/10.1007/s11665-011-0083-1
24. Davis R, Singh A, Debnath K et al (2021) Surface modification of medical-grade Ni55.6Ti44.4 alloy via enhanced machining characteristics of Zn powder mixed-μ-EDM. Surf Coatings Technol 425:. https://doi.org/10.1016/j.surfcoat.2021.127725
25. Ivanov A, Lahiri A, Baldzhiev V, Trych-wildner A (2021) Suggested research trends in the area of micro-edm—study of some parameters affecting micro-edm. Micromachines 12:. https://doi.org/10.3390/mi12101184
26. Raju L, Hiremath SS (2016) A state-of-the-art review on micro electro-discharge machining. Procedia Technol 25:1281–1288. https://doi.org/10.1016/j.protcy.2016.08.222
27. Zahiruddin M, Kunieda M (2012) Comparison of energy and removal efficiencies between micro and macro EDM. CIRP Ann - Manuf Technol 61:187–190. https://doi.org/10.1016/j.cirp.2012.03.006
28. Cyril J, Paravasu A, Jerald J et al (2017) Experimental investigation on performance of additive mixed dielectric during micro-electric discharge drilling on 316L stainless steel. Mater Manuf Process 32:638–644. https://doi.org/10.1080/10426914.2016.1221107
29. Frey DD, Engelhardt F, Greitzer EM (2003) A role for "one-factor-at-a-time" experimentation in parameter design. Res Eng Des 14:65–74. https://doi.org/10.1007/s00163-002-0026-9
30. Selvamuthu D, Das D (2018) Introduction. In: Introduction to Statistical Methods, Design of Experiments and Statistical Quality Control. Springer Singapore, Singapore, pp 1–16. https://doi.org/10.1007/978-981-13-1736-1
31. Prihandana GS, Mahardika M, Hamdi M et al (2013) Study of workpiece vibration in powder-suspended dielectric fluid in micro-EDM processes. Int J Precis Eng Manuf 14:1817–1822. https://doi.org/10.1007/s12541-013-0243-3
32. Davis R, Singh A, Debnath K et al (2022) Enhanced micro-electric discharge machining-induced surface modification on biomedical Ti-6Al-4V alloy. J Manuf Sci Eng 144:. https://doi.org/10.1115/1.4053110

33. Sahu AK, Mahapatra SS (2020) Performance analysis of tool electrode prepared through laser sintering process during electrical discharge machining of titanium. Int J Adv Manuf Technol 106:1017–1041. https://doi.org/10.1007/s00170-019-04675-1
34. Bhaumik M, Maity K (2018) Effect of different tool materials during EDM performance of titanium grade 6 alloy. Eng Sci Technol an Int J 21:507–516. https://doi.org/10.1016/j.jestch.2018.04.018
35. Chen SL, Lin MH, Chen CC, Ou KL (2008) Effect of electro-discharging on formation of biocompatible layer on implant surface. J Alloys Compd 456:413–418. https://doi.org/10.1016/j.jallcom.2007.02.055
36. Thirumalaikumarasamy D, Shanmugam K, Balasubramanian V (2014) Comparison of the corrosion behaviour of AZ31B magnesium alloy under immersion test and potentiodynamic polarization test in NaCl solution. J Magnes Alloy 2:36–49. https://doi.org/10.1016/j.jma.2014.01.004
37. Yin Z-Z, Qi W-C, Zeng R-C et al (2020) Advances in coatings on biodegradable magnesium alloys. J Magnes Alloy 8:42–65. https://doi.org/10.1016/j.jma.2019.09.008
38. Seyfi M, Fattah-alhosseini A, Pajohi-Alamoti M, Nikoomanzari E (2021) Effect of ZnO nanoparticles addition to PEO coatings on AZ31B Mg alloy: antibacterial effect and corrosion behavior of coatings in ringer's physiological solution. J Asian Ceram Soc 1–14. https://doi.org/10.1080/21870764.2021.1940728
39. Sezer N, Evis Z, Kayhan SM et al (2018) Review of magnesium-based biomaterials and their applications. J Magnes Alloy 6:23–43. https://doi.org/10.1016/j.jma.2018.02.003
40. Attia GH, Moemen YS, Youns M et al (2021) Antiviral zinc oxide nanoparticles mediated by hesperidin and in silico comparison study between antiviral phenolics as anti-SARS-CoV-2. Colloids Surfaces B Biointerfaces 203:111724. https://doi.org/10.1016/j.colsurfb.2021.111724
41. Hamdi M, Abdel-Bar HM, Elmowafy E et al (2021) Investigating the internalization and COVID-19 antiviral computational analysis of optimized nanoscale zinc oxide. ACS Omega 6:6848–6860. https://doi.org/10.1021/acsomega.0c06046
42. Kim J-Y, Kim D-O, Byeon J-W (2021) Strength and corrosion resistance of Al-alloying layer on AZ31B magnesium alloy fabricated in situ by reactive friction stir processing. Mater Charact 174:111024. https://doi.org/10.1016/j.matchar.2021.111024
43. Gawlik M, Wiese B, Desharnais V et al (2018) The effect of surface treatments on the degradation of biomedical Mg alloys—a review paper. Materials (Basel) 11:2561. https://doi.org/10.3390/ma11122561
44. Gökhan Demir A, Furlan V, Lecis N, Previtali B (2014) Laser surface structuring of AZ31 Mg alloy for controlled wettability. Biointerphases 9:029009. https://doi.org/10.1116/1.4868240
45. Liu Y, Yao W, Yin X et al (2016) Controlling wettability for improved corrosion inhibition on magnesium alloy as biomedical implant materials. Adv Mater Interfaces 3:. https://doi.org/10.1002/admi.201500723
46. King AD, Birbilis N, Scully JR (2014) Accurate electrochemical measurement of magnesium corrosion rates; A combined impedance, mass-loss and hydrogen collection study. Electrochim Acta 121:394–406. https://doi.org/10.1016/j.electacta.2013.12.124
47. Chen M, Chen Y, Zhang W et al (2016) Controlling the corrosion rate and behavior of biodegradable magnesium by a surface-immobilized ultrathin 1-hydroxyethylidene-1,1-diphosphonic acid (HEDP) film. RSC Adv 6:15247–15259. https://doi.org/10.1039/C5RA23228G
48. Curioni M, Scenini F, Monetta T, Bellucci F (2015) Correlation between electrochemical impedance measurements and corrosion rate of magnesium investigated by real-time hydrogen measurement and optical imaging. Electrochim Acta 166:372–384. https://doi.org/10.1016/j.electacta.2015.03.050
49. Bland LG, King AD, Birbilis N, Scully JR (2015) Assessing the corrosion of commercially pure magnesium and commercial AZ31B by electrochemical impedance, mass-loss, hydrogen collection, and inductively coupled plasma optical emission spectrometry solution analysis. Corrosion 71:128–145. https://doi.org/10.5006/1419